

Absolute Measurement of Domain Composition and Nanoscale Size Distribution Explains Performance in PTB7:PC₇₁BM Solar Cells

Brian A. Collins, Zhe Li, John R. Tumbleston, Eliot Gann, Christopher R. McNeill, and Harald Ade*

The importance of morphology to organic solar cell performance is well known, but to date, the lack of quantitative, nanoscale and statistical morphological information has hindered obtaining direct links to device function. Here resonant X-ray scattering and microscopy are combined to quantitatively measure the nanoscale domain size, distribution and composition in high efficiency solar cells based on PTB7 and PC₇₁BM. The results show that the solvent additive diiodooctane dramatically shrinks the domain size of pure fullerene agglomerates that are embedded in a polymer-rich 70/30 wt.% molecularly mixed matrix, while preserving the domain composition relative to additive-free devices. The fundamental miscibility between the species – measured to be equal to the device's matrix composition – is likely the dominant factor behind the overall morphology with the additive affecting the dispersion of excess fullerene. As even the molecular ordering measured by X-ray diffraction is unchanged between the two processing routes the change in the distribution of domain size and therefore increased domain interface is primarily responsible for the dramatic increase in device performance. While fullerene exciton harvesting is clearly one significant cause of the increase owing to smaller domains, a measured increase in harvesting from the polymer species indicates that the molecular mixing is not the reason for the high efficiency in this system. Rather, excitations in the polymer likely require proximity to a pure fullerene phase for efficient charge separation and transport. Furthermore, in contrast to previous measurements on a PTB7-based system, a hierarchical morphology was not observed, indicating that it is not necessary for high performance.

1. Introduction

Due to continuing substantial improvements in device performance, organic photovoltaics (OPV) are quickly gaining interest as a potential source of renewable and economically viable electric energy. Recently, the power conversion efficiency (PCE) for solar cells based on solution-processable blends of conjugated polymers and fullerenes has surpassed 8% with the materials PTB7 and PC₇₁BM. This achievement has been a culmination of systematic enhancement of the polymer material's energy levels and side chains^[1,2] as well as optimization of the interfaces of these materials with device electrodes.^[3] The use of the C₇₀-based fullerene compared with the more traditional C₆₀ allotrope enhances photoabsorption over a large energy range, allowing the more efficient harvesting of solar energy.

It is well known, however, that the nano-to-mesoscale morphologies of these blends are also critical for the performance of these devices. For example, OPVs are thought to require a co-continuous phase-separated morphology of electron donor and acceptor materials for efficient charge transport with domain size of ~10 nm envisioned to be an ideal match to the diffusion length of the excitons created upon photoabsorption. Polymer crystallinity as measured with X-ray diffraction has also been

shown to be beneficial to device performance in some systems as absorption and charge transport are both enhanced in crystalline portions of the material.^[4–6] Furthermore, it has been shown that non-crystalline portions of these materials mix at the molecular level.^[7–13] The impact of polymer–fullerene miscibility, however, is not well understood, largely because it is difficult to quantitatively measure composition in actual devices. Although PTB7:PC₇₁BM-based devices currently hold the record in OPV performance, they seem to contain very low levels of crystallinity, potentially reducing the impact of this parameter.^[14] With respect to domain size, there have been conflicting results in the literature regarding the effect of the additive diiodooctane (DIO). While energy-filtered transmission electron microscopy (EFTEM) tomography has suggested DIO reduces the domain size,^[14] Chen et al. reported

Dr. B. A. Collins, Dr. J. R. Tumbleston,
E. Gann, Prof. H. Ade
Department of Physics
NCSU, Raleigh, NC 27695-8202, USA
E-mail: harald_ade@ncsu.edu
Dr. Z. Li
Cavendish Laboratory
University of Cambridge
Cambridge, UK
Dr. C. R. McNeill
Department of Materials Engineering
Monash University
Clayton, Victoria 3800, Australia



DOI: 10.1002/aenm.201200377

an increase in domain size.^[15] Chen et al. further reported that the domain composition changes and forms a hierarchical morphology with use of the additive,^[15] potentially making the average domain size less important. Since neither of these studies specified the statistics of domain size distribution nor the actual domain compositions, the precise origin of the performance enhancement in these devices achieved with solvent additives remains elusive. In fact, this lack of quantitative information on morphology is rather general to polymer and small molecule-based devices and stems from a paucity of characterization tools with the necessary sensitivity, resolution and quantitative nature.

Resonant soft X-ray scattering (R-SoXS) experiments have recently been demonstrated to overcome some of these problems, probing structure down to the nanometer length scale but so far only with qualitative information on composition.^[15–18] Combined with X-ray spectromicroscopy, we extend the capability of R-SoXS characterization to enable quantitative measurement of domain composition and size distribution to domains as small as a few nanometers. Applying this methodology to the material system PTB7:PC₇₁BM, we show that the morphology of this system is comprised of a pure amorphous fullerene phase with a large size distribution, dispersed in an overwhelmingly amorphous matrix whose mixed composition of 70/30 (PTB7/PC₇₁BM) wt.% is in agreement with the thermodynamic miscibility of these materials, suggesting miscibility is a major driving factor of the morphology. This conclusion contrasts with a previous report in which the distribution of scattering intensity was interpreted as hierarchical morphologies in PTB7:PC₆₁BM.^[15] In our study, the effect of the DIO additive is revealed to shrink the fullerene dispersions without altering composition. Combining this information with component analysis of the devices' quantum efficiency indicates that

excitons generated in the smaller fullerene agglomerates are more efficiently dissociated. Furthermore, the quantum efficiency in the spectral range where the polymer absorbs also significantly increases despite the absence of change in the chains' local environment or ordering when DIO is added. Thus, extended charge separation via molecularly dispersed fullerene molecules present in both films may be rather inefficient, suggesting molecular miscibility and mixing is not beneficial to device function. The capability to quantitatively measure domain size, composition, and material crystallinity simultaneously within a film is, therefore, critical for understanding fundamental optoelectronic processes in these materials as well as optimizing device performance.

In Section 2, we first outline the improvement of device performance with the additive, resolving the improvement into components originating in the fullerene versus the polymer species. Next the ordering of both the polymer and fullerene are investigated via X-ray diffraction. Finally, to investigate domain morphology and composition, we first use spectromicroscopy to quantitatively probe the large-scale structure and subsequently use resonant scattering to extend characterization to the nanometer scale. The origin of this morphology and its implications for device function are discussed in Section 3.

2. Results

2.1. Device Characteristics

Figure 1 presents the device properties of the 1:1.5 by weight PTB7:PC₇₁BM blend devices (chemical structures in

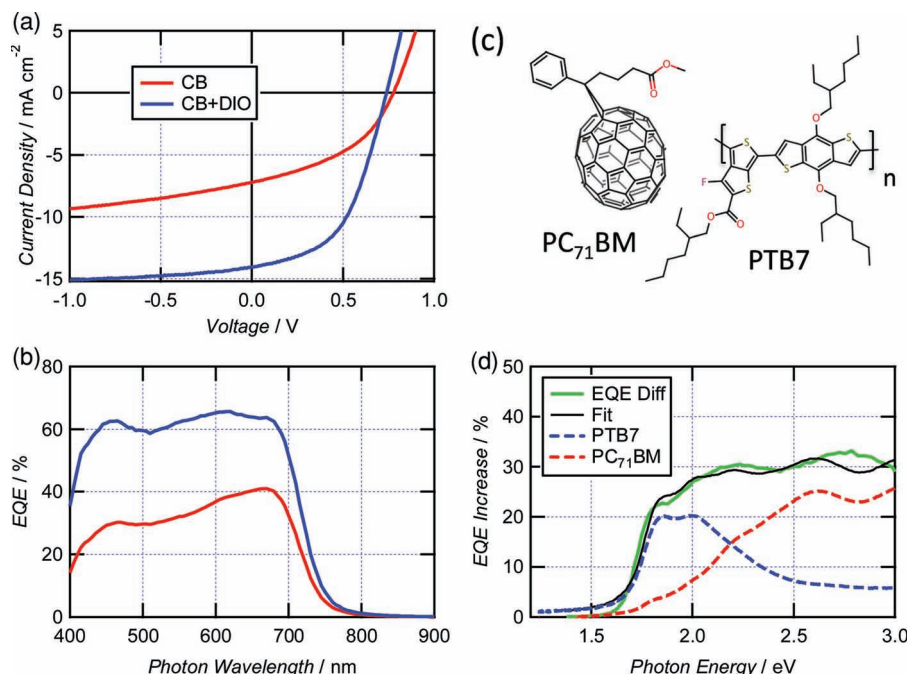


Figure 1. Device and material characterization: (a) Current density vs. applied voltage of the PTB7:PC₇₁BM devices under AM1.5 illumination, (b) external quantum efficiency, (c) material chemical structures, and (d) difference in quantum efficiency between the two devices superimposed by a fit from a linear combination of UV–visible absorption spectra from pristine films of each molecule.

Figure 1c) cast from chlorobenzene (CB) solutions without or with 3 volume% DIO as additive (this point forward labeled “CB” and “CB+DIO” samples). Both device performance (Figure 1a) and external quantum efficiency (EQE, Figure 1b) improve drastically with the addition of DIO, similar to the original study on this effect.^[2] In fact, the EQE and device parameters as outlined in Table 1 are nearly identical to those reported previously^[2]—especially to the CB+DIO device where only the fill factor is different and fully accounts for the difference in efficiency between the two studies. The lower fill factors in our devices may result from unoptimised contact to electrodes that reduce the internal electric field in the device.^[3] The major differences between the two samples in this study are a doubling of the short circuit current and a relatively modest 19% gain in the fill factor resulting in a more than doubling of the efficiency.

To investigate the source of this gain in solar harvesting, the differential EQE spectrum ($\text{EQE}_{\text{CB+DIO}} - \text{EQE}_{\text{CB}}$) was fit to a linear superposition of the pure UV-visible absorbance for each component material and is presented in Figure 1d. This simple analysis allows for a rough calculation of the relative gain in efficiency originating from absorption by the two molecular species. Interference effects in the device were simulated using prior established methods,^[19–22] but did not appear to affect this analysis substantially (see Supporting Information for details). The simulations also showed that reorganization of the lateral morphology would not affect the absorption of the two species, indicating that any gains in the EQE must be from

Table 1. Device parameters: $\text{PCE} = J_{\text{sc}} \cdot V_{\text{oc}} \cdot \text{FF} / I_0$, where incident intensity $I_0 = 100 \text{ W m}^{-2}$.

| Sample | J_{sc} [mA/cm ²] | V_{oc} [V] | FF [%] | PCE [%] |
|--------|--|------------------------|-----------|------------|
| CB | 7.2 | 0.78 | 43 | 2.4 |
| CB+DIO | 14.1 | 0.74 | 51 | 5.3 |

increased exciton dissociation, separation, or charge transport. The resulting relative efficiency gains of 42% for the polymer versus 58% for the fullerene show that the increased efficiency is preferentially from charges originating from PC₇₁BM absorption. This is an important result as most morphological optimizations in the past have focused on the contribution of the polymer and suggests a closer look at fullerene morphology is also warranted in these systems.

2.2. X-Ray Diffraction

As a change in crystallinity has been linked to device performance in multiple material systems, we probed this aspect using grazing incidence wide angle X-ray scattering (GIWAXS) at beamline 7.3.3 of the ALS^[23] with primary results presented in Figure 2. The 2D data in Figure 2a,b, as well as the profiles in Figure 2c,d, reveal patterns very similar to those reported previously for these films.^[14,15,24] The variation of the intensities

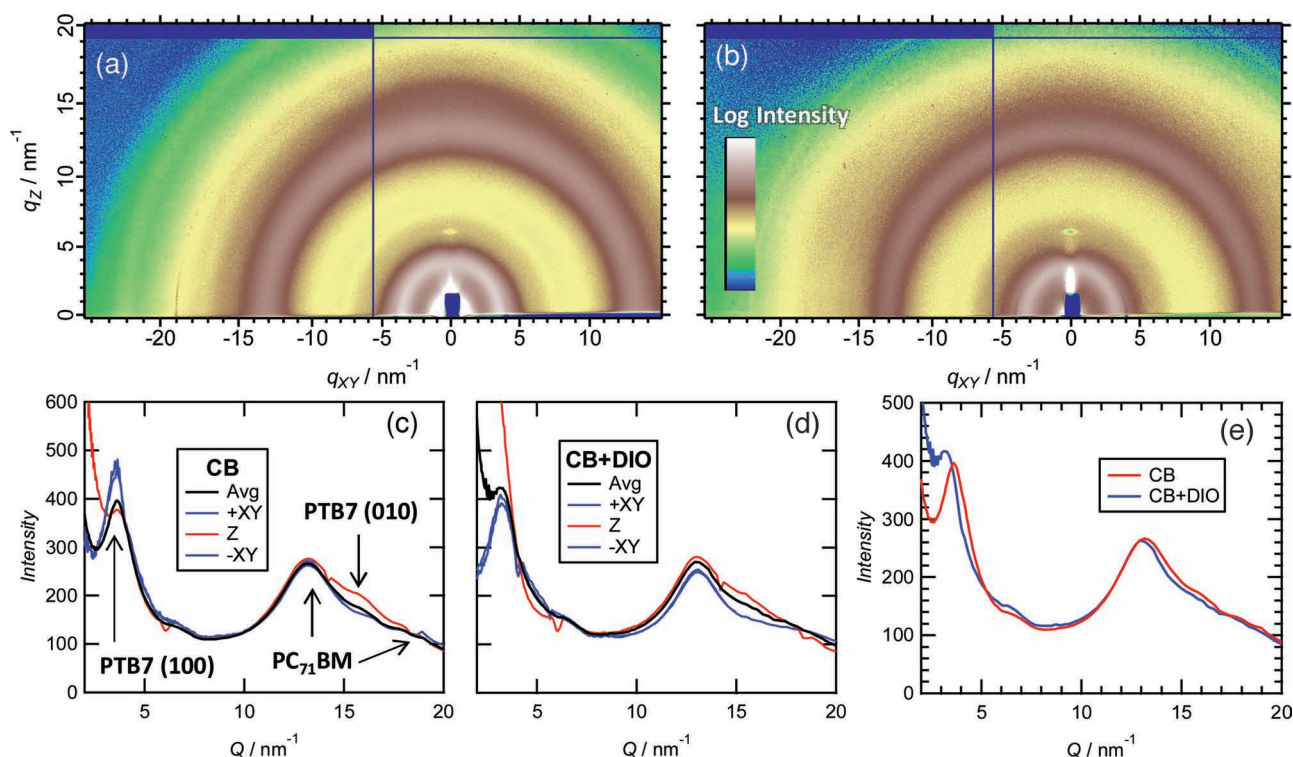


Figure 2. Grazing incidence X-ray scattering study: Panels (a), and (b) show background subtracted CCD output of the CB and CB+DIO samples, respectively. (c) and (d) are $\pm 10^\circ$ sector profiles along the directions specified in the legend and circularly averaged profiles from (a) and (b), respectively. The sharp dip in Z-profiles at -6 nm^{-1} is from a background subtraction artifact. (e) Circularly averaged profiles of the two samples compared directly. Detailed analysis is described in the Supporting Information.

of the polymer reflections with azimuth (shown in the sector profiles of Figure 2c and 2d) confirm the preferential orientation of the polymer aromatic planes of the crystallites is 'face-on' with the substrate and occurs in roughly equal levels in the two samples.

Figure 2e compares the circularly averaged profiles of the two samples. The plots overlap nearly perfectly, demonstrating that the crystallinity of the film changes very little when DIO is added to the casting solution. The only significant difference is in the position of the PTB7 (100) reflection, which represents the lamellar spacing. A decreased peak position indicates that the lamellar spacing increased when DIO is added to the solution. The profiles were fit to a series of Lorentz functions on a double exponential background (see Supporting Information) and confirm that the spacing changes from 17.1(1) Å without DIO to 18.9(1) Å with the additive. No other change of d-spacing was detected, and all other d-spacing values of polymer and fullerene (see Table S1) correspond quantitatively with those reported earlier.^[14,15,24] It is difficult to hypothesize any major effect to devices from the change in lamellae spacing measured here, since charge generation or transport is not thought to occur in this direction of a polymer crystal.

To assess the level of crystallinity, the peak area and coherence ($2\pi/\text{FWHM}$) – which roughly corresponds to crystallite population and size, respectively – were analyzed from the fits. No significant difference between the two samples was detected for both parameters of all analyzed peaks (see Figure S2). In the polymer, the PTB7 (100) peak area is substantial but has a coherence of only 30 Å, resulting in less than two lamellar spacings per 'crystallite'. For the PTB7 (010) π -stacking reflection – the direction corresponding to charge transport – the measured coherence results in approximately five stacked molecules but with the fitted values of coherence and peak area agreeing with zero due to the surrounding fullerene reflections (See Figure S2). All fullerene peaks result in packing coherences of ~ 20 Å or less, but with a measured (100) d-spacing of 9.7(1) Å, this only corresponds to a 'crystal' of a few molecules. This coherence length is typical of most polymer/fullerene blends and has been used to postulate a lack of fullerene crystallinity in these films.^[25] These results agree with previous studies demonstrating that the crystallite population is very small.^[14]

2.3. Resonant Microscopy and Thermodynamic Miscibility

Since the crystallinity is very low and does not change between the samples, it cannot be the reason for the dramatic change in device performance. Therefore, the overall morphology and composition was investigated using spectromicroscopy with a scanning transmission X-ray microscope (STXM) at the 5.3.2.2 beamline of the Advanced Light Source.^[26] Due to diverse molecular resonances of the two components, an image of a film acquired at multiple X-ray energies can be quantified into composition at each pixel via knowledge of each material's mass absorption spectra as calculated from near edge X-ray absorption fine structure (NEXAFS) measurements (see Figure 3a).^[27–30] Presented in Figure 3, the composition maps of the two films reveal extremely different morphologies with ~ 200 nm sized fullerene dispersions in a mixed matrix for the

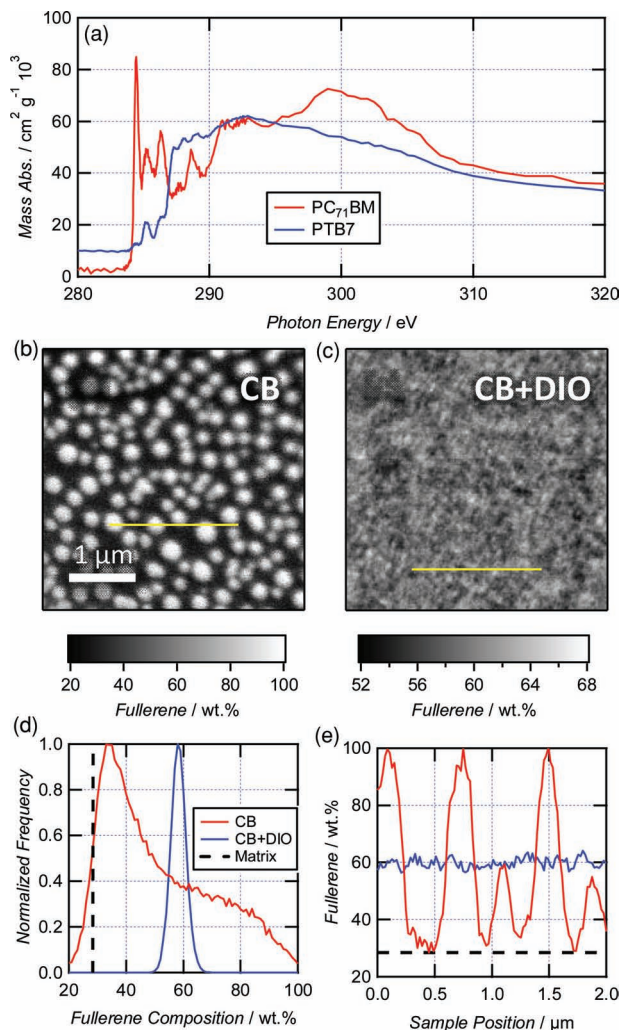


Figure 3. Resonant microscopy: (a) NEXAFS spectra of the component materials demonstrating the nature of the contrast. (b) & (c) Film composition maps (same magnification) of the CB and CB+DIO films, respectively, obtained from imaging at energies 284.4 eV, 320 eV and 350 eV in (a). (See Supporting Information for details.) (d) Histograms of (b) & (c). (e) Line profiles taken from the yellow lines in (b) & (c). The black dashed lines in (d) & (e) represent the measured composition of the matrix phase in the CB sample.

CB samples compared to a much finer texture in the CB+DIO sample, in agreement with AFM data (Figure S4) and EFTEM tomography.^[14] The histogram and line profiles in Figure 3d,e show that the matrix in the CB sample is 30(2) wt.% fullerene whereas the fullerene dispersions are pure to within an uncertainty of 2 wt.%, similar to the domain compositions of MDMO-PPV/PC₆₁BM blends.^[28] Although the theoretical resolution limit of the microscope under ideal operating conditions is 31 nm, quantitative measurements become unreliable in features far larger due to the point spread function of the X-ray beam artificially reducing the measured purity of the domains.^[30] (See the round-topped fullerene dispersions in Figure 3e, for example.) The features seen here are at the limit of accurate compositional analysis, and this is the first time the

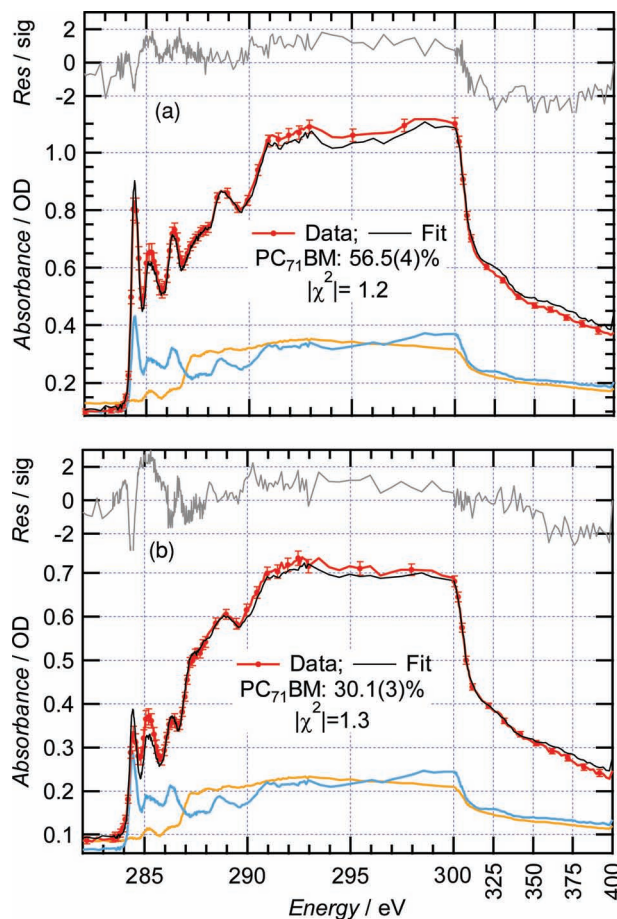


Figure 4. PTB7 miscibility with PC₇₁BM: Panel (a) and (b) show composition measurement of as cast blend film and one annealed at 140 °C for 95 hours in an inert environment, respectively. Red lines/symbols are NEXAFS data/uncertainty, black lines are fits, and grey lines are residuals divided by the uncertainty. Yellow and blue lines are PTB7 and PC₇₁BM reference spectra used in the fit and plotted on a separate Y-axis for clarity.

domain composition of device active layers has been measured in such a high performing material system. By comparison, the CB+DIO sample is either nearly fully mixed or has domains that are smaller than the resolution limit of the X-ray microscope. The composition analysis on this sample, however, cannot be conclusive as the size of the morphology imaged with STXM is far below the resolution limit for quantitative analysis.

To assess the role that thermodynamics plays in the composition of the domains, the molecular miscibility was measured as done previously for P3HT^[7] following the detailed analysis outlined elsewhere.^[30] Figure 4 presents fitted NEXAFS spectra for blend films as cast and annealed (at 140 °C) to compositional equilibrium. The annealed films developed many-micron sized PC₇₁BM crystals as seen in other studies,^[7,12,13] which gradually depleted the surrounding film. The statistical average miscibility from multiple measurements resulted in 29(1) wt.% PC₇₁BM in PTB7 – the same value as measured in the matrix of the as-cast CB films. This result suggests that the initial fullerene composition of 60 wt.% in solution is high enough for spontaneous phase separation (above the binary spinodal) and

there is sufficient time and mobility during solvent evaporation for the matrix to reach the thermodynamic limit, which should in all cases be a lower bound for the fullerene concentration as the solvent concentration diminishes to zero. A miscibility this high may be important for electron transport in the matrix as it is well above the percolation threshold of ~20 wt.% demonstrated recently by Vakhshouri et al. in electron transport measurements through PC₆₁BM in regiorandom P3HT.^[31]

2.3. Resonant Scattering

To probe morphology below the resolution limit of X-ray spectromicroscopy, we conducted R-SoXS experiments on the same two films investigated with diffraction and microscopy. Scattering intensity arises from structure in the film through the contrast function defined as $C = |\Delta\delta^2 + \Delta\beta^2|E^4 = \Delta n^2 E^4$ where $n = 1 - \delta + i\beta$ is the materials' complex index of refraction and E is the photon energy. Displayed in Figure 5a, this function can be calculated from the NEXAFS measurements (Figure 3a).^[32] There are two primary ways that structure in the film can cause scattering: roughness/thickness variations through the vacuum contrast (blue and red dashed lines Figure 5a), and material domains (black line Figure 5a). To probe material domains, we conducted the scattering experiment at 282.5 eV where the vacuum contrast of both components are minimized relative to the material contrast (green arrow Figure 5a). Notably, using this energy takes advantage of the materials' phase (i.e. δ) contrast rather than absorption (β) contrast used in STXM and thus largely avoids the associated radiation damage effects on the sample and fluorescent background that occurs when core-holes are created.

The results of the R-SoXS experiment are presented in Figure 5b, each film showing a well-defined broad peak, which were each successfully fit to Voigt peak functions with a $\log(q)$ axis (a second small peak for the shoulder in the CB sample). Due to the large polydispersity of the domain sizes as evident in the STXM images, any form factor from the dispersions themselves will be washed out, leaving only the structure factor information.^[33] These peaks, therefore, represent domain spacing at $d = 2\pi/q$ (see top axis of Figure 4b), which is reduced considerably in the presence of the DIO additive. Particularly important to characterizing this system was the use of the proper X-ray energy in reducing vacuum contrast. Scattering profiles acquired at 272 eV, where vacuum contrast dominates, show a double peak in the CB+DIO sample (Figure S6), which could erroneously be interpreted as a hierarchical structure or a morphology with multiple lengthscales. This highlights that a judicious choice of photon energy is necessary in resonant scattering.

The scattering profiles can be processed further to extract the domain purity of an assumed two phase system through the total scattering intensity (TSI) as first shown by Porod and therefore also referred to as Porod's invariant.^[33–35]

$$\text{TSI} = \int_0^\infty I(q)q^2 dq = 2\pi^2 \Delta\rho_{12}^2 v_1 v_2 V \quad (1)$$

where $\Delta\rho_{12}$ is the difference in electron density between the two phases, v_i is the volume fraction of each domain and V is the total illuminated volume. This quantity is insensitive to

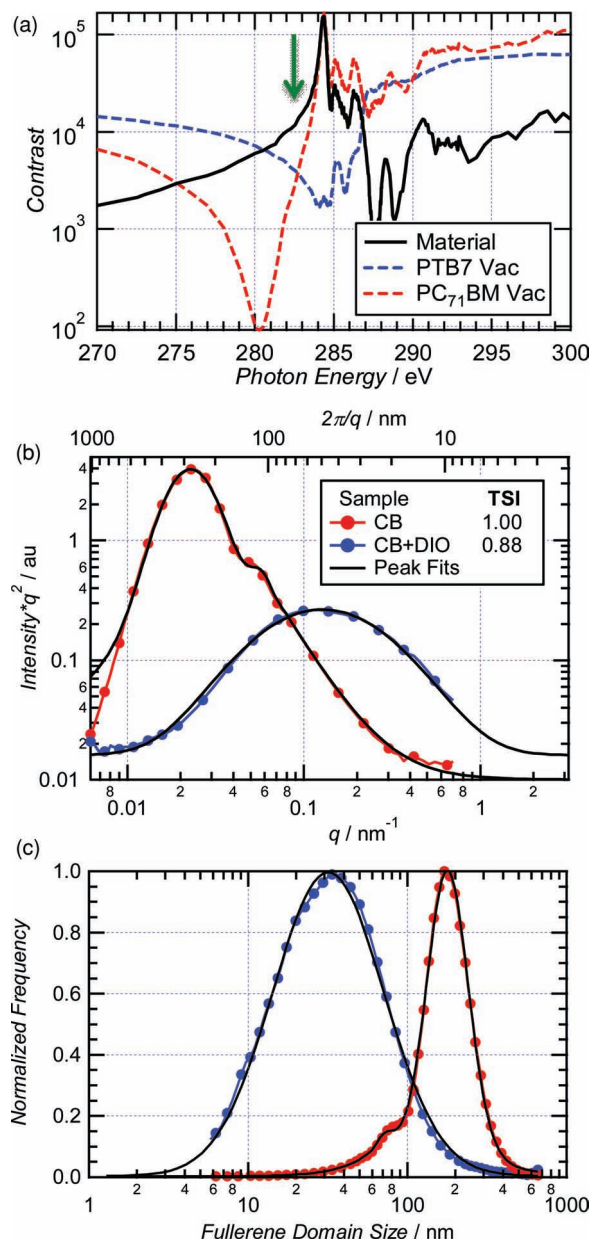


Figure 5. R-SoXS study: (a) Contrast functions ($\Delta n^2 E^4$) for each material with vacuum ($n = 1$) and between each material calculated from NEXAFS measurements in Figure 3a. The assumed density used in the calculation was 1.12 and 1.25 g/cm³ for PTB7 and PC₇₁BM, respectively based on similar materials.^[46,47] Green arrow indicates where data was acquired. (b) Azimuthally integrated scattering profiles with associated peak fits and calculation of the Total Scattered Intensity (TSI). (c) Normalized histogram of scattering intensity versus fullerene domain size from calculations described in the text. Extra scattering from interfaces in the CB sample (red curve) below ~80 nm likely spuriously enhances the apparent domain population at this size scale.

morphology as domains of different sizes scattering to different angles (q). What does affect the TSI is domain contrast, which is therefore an important measure of the domain purity. We extend equation 1 for resonant X-rays through the following conversion:

$$\rho = \frac{f_1 - if_2}{V} = \sum_j n_j (f_{1j} + if_{2j}) = \alpha E^2 (\delta - i\beta) \quad (2)$$

where $f_1 - if_2$ are the complex elemental scattering factors, n_j are the number densities for the j^{th} element in each component molecule, and α is a factor containing only universal constants (see Supporting Information). The left equality in equation 2 comes from the fact that the scattering factor is equivalent to the effective number of electrons that scatter, while the middle equality converts from atomic view to that of a molecule. The final equality converts from scattering factors to optical constants. Thus

$$\Delta \rho_{12}^2 = \alpha^2 E^4 \Delta n_{12}^2 = \alpha^2 C_{12} \quad (3)$$

where the subscripts indicate contrast between domains (not materials). If the materials are mixed within the domains, this contrast will be reduced accordingly, and so will the TSI.

As shown in the legend of Figure 5b, the TSIs from the two samples investigated differ by only 12% as calculated from equation 3. The illuminated volume V was measured to be the same for both samples (see Supporting Information). As Δn scales with purity and the volume fraction of the domains has to be very similar, this difference in the TSI means an approximately $\sqrt{1.00} - \sqrt{0.88} = 6\%$ difference in relative phase purity between the two samples. Remarkably, this implies that the relative domain composition is nearly identical in both samples and only the size distribution has changed.

The nature of the domain interface can also be probed using Porod's law for which the high- q limit of the scattering profile follows a power law.^[33,35,36] Smooth, sharp interfaces result in an intensity fall off of q^{-4} . Fractal interfaces fall off slower (the effective interface area grows as smaller length scales are probed increasing scattering), while diffuse interfaces fall off faster (more mixing produces less scattering). This analysis was possible on the CB sample, where fits in the Porod region resulted in a power of ~ -4.5 (Figure S5), suggesting diffuse interfaces—in contrast to analysis in P3HT:PC₆₁BM where the power-law scaling with q is less than -4 ,^[10] and thus the interfaces in P3HT:PC₆₁BM are “fractal” due to crystallite boundaries. The small quantitative reduction of the TSI measured here between the samples is possibly due to this interface diffusiveness, where the much smaller domains in the CB+DIO sample have a higher interface-to-volume ratio, and therefore the average purity over the entire domain would appear to decrease slightly. An alternative explanation may be that, although the fullerene dispersions are also pure in the CB+DIO sample, the matrix is slightly enriched in PC₇₁BM which is held in solution longer by the DIO and eventually trapped in the frozen PTB7-rich matrix.

Having established that the domain compositions for both samples are essentially equal, the intensity profiles can be inverted into real space histograms of fullerene domain diameter (conversion from spacing to diameter in supporting information). It is important to note that this simple inversion can only be accomplished with independent confirmation that domain form factors do not contribute to the scattering as is the case here. These scattering intensity histograms, representing the volume distribution of domain sizes, are plotted in Figure 5c revealing a monomodal distribution rather than

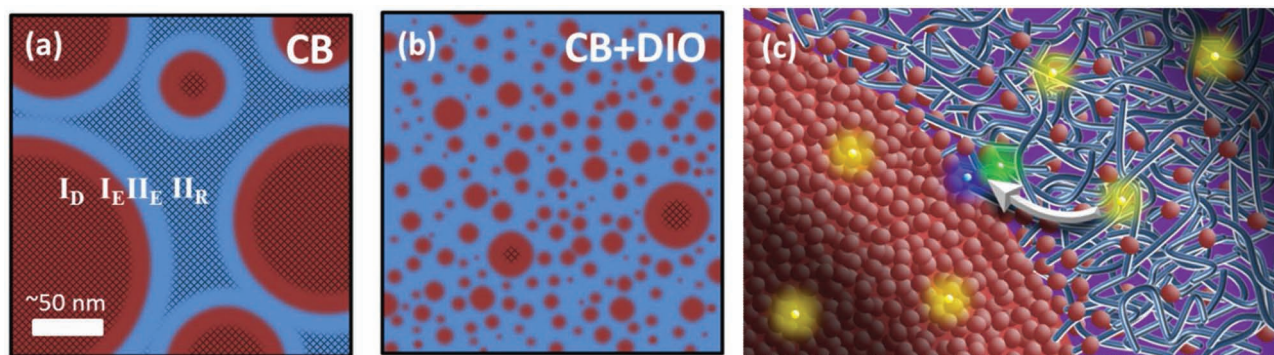


Figure 6. Morphological and operational schematic: (a) CB film and (b) CB+DIO film. Region I (red) is the pure PCBM agglomerate phase and Region II (blue) is the mixed matrix phase. Regions I_E and II_E are those where the photovoltaic effect is most efficient. Region I_D is a region that is dead due to exciton relaxation and Region II_R is where geminate recombination is high. (c) Molecular view at an interface between Regions I and II. Red circles are PC₇₁BM molecules and blue lines represent PTB7 chains. Yellow dots are excitons while purple and green dots are separated electrons and holes, respectively. Excitons created in the darker regions lie outside the efficient zone and will either relax back to the ground state or recombine geminately.

bimodal or hierarchical. The difference in domain size distribution between the samples is stark, with a dominant domain size of 177 nm in the CB sample reduced to that of 34 nm when DIO is added. The latter size is far more amenable to efficient dissociation of excitons created in the fullerene agglomerates at a domain interface and is too small to be imaged by the STXM, explaining the results in Figure 3c. This distribution is fairly wide, however, with some domain diameters well below 10 nm while others are 100s of nm in size. A tighter distribution around 10 nm may improve exciton capture of the PCBM further.

3. Discussion

The combined three techniques used here to assess film morphology clearly show that both films are composed of pure fullerene droplet-like dispersions in a 30:70 wt.% mixed matrix as shown in Figure 6. Evidently, the thermodynamic miscibility measured between molecular species is the dominant driving force and trumps any mediating influence of the additive on domain composition. The effect of the additive is primarily to modify the kinetics of film solidification, helping to better disperse the excess fullerene agglomerates in the matrix that has a composition near the thermodynamic equilibrium. The importance of the miscibility in controlling domain composition in this system contrasts with that of P3HT:PC₆₁BM, where significantly higher fullerene compositions are metastable beyond the thermodynamic miscibility of the two species.^[37,38] The GIWAXS measurements additionally suggest that both phases are overwhelmingly amorphous. It is conspicuous that such large and pure agglomerates of fullerenes wouldn't crystallize as seen in P3HT:PC₆₁BM systems,^[39] but as no thermal annealing was used in the processing, it is likely that the mobility of fullerenes is low and the solidification fast enough to prevent crystallization. This type of morphology with large pure fullerene phases in a mixed matrix has been reported earlier for MDMO-PPV:PC₆₁BM blends.^[28] In contrast to the hierarchical structure reported by Chen and coworkers

in PTB7:PC₆₁BM,^[15] a simple two-domain model describes our data very well. This also agrees with EFTEM tomography of PTB7:PC₇₁BM—a more direct but qualitative measurement with respect to composition.^[14] Our results additionally depart from the morphological trends deduced in the previous work by Chen and coworkers^[15] where their results suggested the dominant domain size to increase from ~180 nm to ~230 nm as well as the domain purity to decrease by a factor of 4 when DIO was added to the solution. These conclusions relied on Guinier analysis of radius of gyration which requires isolated domains or polymers^[33] (inappropriate as evidenced by the STXM images) and composition analysis via the pair distribution function maximum, which is difficult to interpret as it is convoluted with domain polydispersity.^[33] Since the study by Chen *et al.* used the PC₆₁BM fullerene, which has been shown to have very different miscibilities with some polymers than PC₇₁BM^[12,13] a direct comparison is not possible as the systems could develop different morphologies.

Interpreting the change in device performance in terms of the morphological changes depicted in Figure 6 is relatively straightforward for the fullerene species. The dramatic decrease in the fullerene domain size will result in a significant increase in exciton harvesting from the fullerene phase, an outcome which is supported by the enhanced photocurrent derived from the fullerene species relative to the polymer as seen in analysis of the differential EQE spectra. An improved efficiency from the fullerene species has been noted recently in a material system where the polymer performed uncharacteristically poorly, but the morphology was not fully characterized.^[40] The connection between morphology and performance is also particularly clean in this case because we have shown that in the very same film, neither the crystallinity nor the composition but only the domain size distribution changes. Thus much of the improvement in J_{SC} can be interpreted in terms of increased exciton dissociation yield.

What is less obvious is the reason for the increase in the quantum efficiency corresponding to light absorption by the polymer phase. While we determine that 58% of the overall increase in quantum efficiency is due to improvement in the

fullerene photocurrent generation, the 42% increase in polymer photocurrent generation is not insignificant. In fact, the higher solar photon flux at energies absorbed by the polymer relative to those of the fullerene would likely rebalance the impact from the two species, making the efficiency improvement due to polymer component potentially more important. We note that there is a moderate increase in fill factor in the CB+DIO device compared to the CB device, which could reflect an improvement in charge separation efficiency. Indeed, we have recently observed a stronger field-dependence of photocurrent generation in the polymer relative to the fullerene in CB devices that is absent in CB+DIO devices made from the same batch of materials used here.^[41] Thus the solvent additive appears to assist the separation of charge following polymer exciton dissociation into the charge transfer state.

Our morphological measurements show that neither the local environment nor the ordering of the polymer changes with the presence of the DIO additive. Rather, the morphology change is in each polymer molecule's proximity to the fullerene agglomerates along with an increase of interfacial area between the two phases (see Figure 6). One hypothesis regarding the increased polymer photocurrent generation is, therefore, that direct access of polymer chains to a fullerene agglomerate facilitates efficient charge separation of electron-hole pairs. The importance of fullerene clusters in promoting extended charge separation has been previously highlighted by Veldman et al.^[42] where suppression of charge transfer photoemission was linked to the formation of phase-separated fullerene domains. A physical argument behind why access to fullerene agglomerates might be essential is that for dispersed fullerene molecules in the matrix, the energy offset between the two species' lowest unoccupied electron orbitals (LUMOs) is too close to the polymer's exciton binding energy for efficient charge separation. A recent report suggested that fullerene agglomerates have a deeper LUMO (a higher electron affinity) than dispersed molecules.^[43] Charge transfer states in large regions of the matrix (Region II_R in Figure 6a), therefore, may not have enough excess energy to separate into free charges, experiencing a higher rate of geminate recombination and a higher field-dependence for charge separation. This could easily account for the increase in fill factor and increased quantum efficiency from the polymer as well and demonstrate the powerful impact of film morphology on device performance. Regardless of the underlying physical mechanism, however, it is clear that the mixed phase measured here is not a reason for the increased efficiency in this material system, suggesting that molecular miscibility may not always have a positive effect on organic solar cell performance.

4. Conclusion

In combination, these complementary resonant X-ray techniques applied to the same film reveal critical quantitative statistical information on the nano to mesoscale morphology which has until now been unattainable by any means. Specifically, the domain size distribution and the absolute domain

composition have been measured in PTB7:PC₇₁BM blend films by combining resonant spectromicroscopy and scattering. The results reveal a simple dispersion and matrix morphology rather than a hierarchical structure, and that the matrix composition is equal to the thermodynamic miscibility between the components. Importantly, the domain composition and crystallinity are shown to be essentially unchanged with the addition of DIO into the casting solution, while the domain size dramatically decreases. This decrease is linked to improved exciton harvesting in the fullerene and charge separation in the polymer and suggests a mixed phase is not beneficial to device performance but rather polymer access to pure fullerene agglomerates is important for efficient charge separation in this system. For the first time the total scattering intensity has been interpreted for use in the case of resonant X-rays where molecular contrast rather than electron density contrast dominates. This technique allows for the increasingly quantitative measurements required for probing organic blend films in general and organic solar cells in particular, helping to guide a more refined understanding of device function.

5. Experimental Section

PTB7 was supplied by 1-Material (Batch SX6-037P) with a Mw of ~200 kg mol⁻¹ and PDI of ~4. PC₇₁BM was supplied by Nano-C. All films investigated via X-rays were cast onto NaPSS-coated glass substrates. Solar cells were fabricated on ITO-coated glass covered with a ~60 nm layer of PEDOT:PSS (poly(3,4-ethylenedioxythiophene):polystyrene sulfonic acid). NaPSS and PEDOT:PSS films were dried at 150 °C for 30 min under flowing nitrogen prior to transfer to a nitrogen glovebox for further processing steps. PTB7:PC₇₁BM (1:1.5 by weight) was spincoated from a chlorobenzene solution (25 total g L⁻¹) either with or without 3 vol% 1,8-diiodooctane as cosolvent to give films ~100 nm thick. Solar cells were completed with the evaporation of a 100 nm thick aluminum top electrode. Component films were cast from chlorobenzene solutions (30 g L⁻¹ for PTB7 and 50 g L⁻¹ for PC₇₁BM) for characterization using UV-vis and NEXAFS spectroscopy.

Current-voltage characteristics of devices were measured with a Keithley 2635 source measure unit under 100 mW cm⁻² simulated AM1.5G (ABET Sun 2000 Class AAA). EQE measurement was performed using a 250 W tungsten halogen lamp (Newport, Simplicity QTH) dispersed through a monochromator (Oriol Cornerstone 130) with a filter wheel used to block higher orders. Light intensities of less than 1 mW cm⁻² were used with the short-circuit current recorded using a Keithley 2635 source measure unit. Light intensity was calibrated with a calibrated photodiode with a beamsplitter and reference diode used to continuously monitor intensity during measurement. UV-vis spectra of the component materials were acquired with a Varian Cary 50 scan spectrophotometer.

GIWAXS measurements were performed at the ALS bending magnet beamline 7.3.3^[23] with 10 keV X-rays at an angle of incidence of 0.09°, which allowed penetration through the entire film. The scattered intensity was collected by an ADSC Quantum 4 CCD. A plastic bag with helium flow minimized air scatter along the entire photon path. Scattering from a NaPSS-coated glass substrate was measured and used to subtract substrate scattering from the signal. Data processing was carried out using the NIKA software package.^[44]

STXM and NEXAFS measurements were performed at the ALS bending magnet beamline 5.3.2.2^[26] using a 240 μm diameter zone plate with an outermost zone-width of 25 nm. Entrance and exit slits were at 50 μm and 25 μm, respectively. Approximately 0.6 Torr of N₂ was bled into a section of the beamline to improve spectral purity. All data was acquired and processed using methods reported elsewhere.^[30]

R-SoXS was conducted at the ALS elliptically polarized undulator beamline 11.0.1.2 with most details of the beamline, experiment and analysis reported elsewhere.^[45] Important parameters are described below in brief. The four bounce order sorter was set to 6° for highest spectral purity. The scattered intensity was recorded by a back illuminated Princeton PI-MTE CCD thermoelectrically cooled to −45 °C. The attenuated beam (via carbon film) was imaged directly by the CCD to give a Gaussian profile with FWHM $\sim 200 \times 300 \mu\text{m}$. The sample-detector distance was measured using diffraction from a drop-cast film of 300 nm polystyrene spheres. A modified version of the NIKA software package was used to: i) subtract background, ii) normalize by the I_0 provided by a gold mesh and photodiode, iii) make solid angle corrections and iv) reduce the data to $I(q)$ profiles. Integrated scattering intensity profiles represent total scattered intensity at a given q . This was accomplished by averaging the data along the azimuth captured by the CCD and subsequently scaling the profiles by q^2 . Scattering from the sample was captured by the CCD as far from the sample as possible ($\sim 170 \text{ mm}$) and with the CCD as close as possible ($\sim 70 \text{ mm}$). The profiles acquired from the two datasets were stitched together for an extended q -range.

Note: An optical modeling study is included to determine the effect of optical interference in a device on the relative absorption of the two components. Details of the GIWAXS analysis, details of the analysis of film composition maps, AFM images, details of the TSI and Porod analyses, and calculations for the R-SoXS histogram are also included. This material is available in the Supporting Information.

Supporting Information

Supporting Information is available from the Wiley Online Library or from the author.

Acknowledgements

STXM Training and beamline support were provided at beamline 5.3.2 by David Kilcoyne. Beamline support at beamline 11.0.1.2 was provided by Anthony Young and Cheng Wang. Work by NCSU was supported by the U.S. Department of Energy, Office of Science, Basic Energy Science, Division of Materials Science and Engineering under Contract DE-FG02-98ER45737. Eliot Gann was also supported by a GAANN Fellowship under the Department of Education. Work at Cambridge University was funded by the Engineering and Physical Sciences Research Council (EP/E051804/1, EP/G031088/1) and in Australia by the Australian Research Council (FT100100275). STXM and NEXAFS data were acquired at beamline 5.3.2 and GIWAXS at beamline 7.3.3. at the Advanced Light Source, Berkeley, which is supported by the Director, Office of Science, Office of Basic Energy Sciences, of the U.S. Department of Energy under Contract No. DE-AC02-05CH11231.

Received: May 28, 2012

Revised: June 22, 2012

Published online: October 1, 2012

- [1] Y. Liang, D. Feng, Y. Wu, S.-T. Tsai, G. Li, C. Ray, L. Yu, *J. Am. Chem. Soc.* **2009**, *131*, 7792.
- [2] Y. Liang, Z. Xu, J. Xia, S.-T. Tsai, Y. Wu, G. Li, C. Ray, L. Yu, *Adv. Mater.* **2010**, *22*, E135.
- [3] Z. He, C. Zhong, X. Huang, W.-Y. Wong, H. Wu, L. Chen, S. Su, Y. Cao, *Adv. Mater.* **2011**, *23*, 4636.
- [4] V. D. Mihailetschi, H. X. Xie, B. de Boer, L. J. A. Koster, P. W. M. Blom, *Adv. Funct. Mater.* **2006**, *16*, 699.

- [5] Y. Kim, S. Cook, S. M. Tuladhar, S. A. Choulis, J. Nelson, J. R. Durrant, D. D. C. Bradley, M. Giles, I. McCulloch, C.-S. Ha, M. Ree, *Nat. Mater.* **2006**, *5*, 197.
- [6] W.-R. Wu, U. S. Jeng, C.-J. Su, K.-H. Wei, M.-S. Su, M.-Y. Chiu, C.-Y. Chen, W.-B. Su, C.-H. Su, A.-C. Su, *ACS Nano* **2011**, *5*, 6233.
- [7] B. A. Collins, E. Gann, L. Guignard, X. He, C. R. McNeill, H. Ade, *J. Phys. Chem. Lett.* **2010**, *1*, 3160.
- [8] N. D. Treat, M. A. Brady, G. Smith, M. F. Toney, E. J. Kramer, C. J. Hawker, M. L. Chabinyc, *Adv. Energy Mater.* **2011**, *1*, 82.
- [9] B. A. Collins, J. Tumbleston, H. Ade, *J. Phys. Chem. Lett.* **2011**, *2*, 3135.
- [10] W. Yin, M. Dadmun, *ACS Nano* **2011**, *5*, 4756.
- [11] D. Chen, F. Liu, C. Wang, A. Nakahara, T. P. Russell, *Nano Lett.* **2011**, *11*, 2071.
- [12] B. A. Collins, Z. Li, C. R. McNeill, H. Ade, *Macromolecules* **2011**, *44*, 9747.
- [13] X. He, B. A. Collins, B. Watts, H. Ade, C. R. McNeill, *Small* **2012**, *8*, 1920.
- [14] M. R. Hammond, R. J. Kline, A. A. Herzing, L. J. Richter, D. S. Germack, H.-W. Ro, C. L. Soles, D. A. Fischer, T. Xu, L. Yu, M. F. Toney, D. M. DeLongchamp, *ACS Nano* **2011**, *5*, 8248.
- [15] W. Chen, T. Xu, F. He, W. Wang, C. Wang, J. Strzalka, Y. Liu, J. Wen, D. J. Miller, J. Chen, K. Hong, L. Yu, S. B. Darling, *Nano Lett.* **2011**, *11*, 3707.
- [16] S. Swaraj, C. Wang, H. Yang, B. Watts, J. Lüning, C. R. McNeill, H. Ade, *Nano Lett.* **2010**, *10*, 2863.
- [17] H. Yan, B. A. Collins, E. Gann, C. Wang, H. Ade, C. R. McNeill, *ACS Nano* **2012**, *6*, 677.
- [18] B. A. Collins, J. E. Cochran, H. Yan, E. Gann, C. Hub, R. Fink, C. Wang, T. Schuettfort, C. R. McNeill, M. L. Chabinyc, H. Ade, *Nat. Mater.* **2012**, *11*, 536.
- [19] N.-K. Persson, H. Arwin, O. Inganäs, *J. Appl. Phys.* **2005**, *97*, 034503.
- [20] J. R. Tumbleston, Y. Liu, E. T. Samulski, R. Lopez, *Adv. Energy Mater.* **2012**, *2*, 477.
- [21] G. F. Burkhard, E. T. Hoke, M. D. McGehee, *Adv. Mater.* **2010**, *22*, 3293.
- [22] S. G. Tikhodeev, A. L. Yablonskii, E. A. Muljarov, N. A. Gippius, T. Ishihara, *Phys. Rev. B* **2002**, *66*, 045102.
- [23] A. Hexemer, W. Bras, J. Glossinger, E. Schaible, E. Gann, R. Kirian, A. MacDowell, M. Church, B. Rude, H. Padmore, *J. Phys. Conf. Ser.* **2010**, *247*, 012007.
- [24] J. M. Szarko, J. Guo, Y. Liang, B. Lee, B. S. Rolczynski, J. Strzalka, T. Xu, S. Loser, T. J. Marks, L. Yu, L. X. Chen, *Adv. Mater.* **2010**, *22*, 5468.
- [25] E. D. Gomez, K. P. Barteau, H. Wang, M. F. Toney, Y.-L. Loo, *Chem. Commun.* **2011**, *47*, 436.
- [26] A. L. D. Kilcoyne, T. Tyliczszak, W. F. Steele, S. Fakra, P. Hitchcock, K. Franck, E. Anderson, B. Harteneck, E. G. Rightor, G. E. Mitchell, A. P. Hitchcock, L. Yang, T. Warwick, H. Ade, *J. Synchrotron Radiat.* **2003**, *10*, 125.
- [27] C. R. McNeill, B. Watts, L. Thomsen, W. J. Belcher, N. C. Greenham, P. C. Dastoor, *Nano Lett.* **2006**, *6*, 1202.
- [28] C. R. McNeill, B. Watts, L. Thomsen, W. J. Belcher, A. L. D. Kilcoyne, N. C. Greenham, P. C. Dastoor, *Small* **2006**, *2*, 1432.
- [29] H. Ade, A. P. Hitchcock, *Polymer* **2008**, *49*, 643.
- [30] B. A. Collins, H. Ade, *J. Electron. Spectrosc.* **2012**, *185*, 119.
- [31] K. Vakhshouri, D. R. Kozub, C. Wang, A. Salleo, E. D. Gomez, *Phys. Rev. Lett.* **2012**, *108*, 026601.
- [32] D. Attwood, *Soft X-rays and Extreme Ultraviolet Radiation, Principles and Applications*, Cambridge University Press, Cambridge, U. K. **2000**.
- [33] H. Brumberger, Ed. *Modern Aspects of Small-Angle Scattering*, Vol. 45, Kluwer Academic Publishers, Dordrecht **1995**.

- [34] G. Porod, *Colloid Polym. Sci.* **1952**, 125, 108.
- [35] *Small Angle X-ray Scattering* (Eds: O. Glatter, O. Kratky), Academic Press, London **1982**.
- [36] G. Porod, *Colloid Polym. Sci.* **1951**, 124, 83.
- [37] C. Müller, T. A. M. Ferenczi, M. Campoy-Quiles, J. M. Frost, D. D. C. Bradley, P. Smith, N. Stingelin-Stutzmann, J. Nelson, *Adv. Mater.* **2008**, 20, 3510.
- [38] D. R. Kozub, K. Vakhshouri, L. M. Orme, C. Wang, A. Hexemer, E. D. Gomez, *Macromolecules* **2011**, 44, 5722.
- [39] E. Verploegen, R. Mondal, C. J. Bettinger, S. Sok, M. F. Toney, Z. Bao, *Adv. Funct. Mater.* **2010**, 20, 3519.
- [40] S. D. Dimitrov, C. B. Nielsen, S. Shoaee, P. Shakya Tuladhar, J. Du, I. McCulloch, J. R. Durrant, *The J. Phys. Chem. Lett.* **2011**, 3, 140.
- [41] T. J. K. Brenner, Z. Li, C. R. McNeill, *J. Phys. Chem. C* **2011**, 115, 22075.
- [42] D. Veldman, O. z. Ipek, S. C. J. Meskers, J. r. Sweelssen, M. M. Koetse, S. C. Veenstra, J. M. Kroon, S. S. v. Bavel, J. Loos, R. A. J. Janssen, *J. Am. Chem. Soc.* **2008**, 130, 7721.
- [43] F. C. Jamieson, E. B. Domingo, T. McCarthy-Ward, M. Heeney, N. Stingelin, J. R. Durrant, *J. Chem. Sci.* **2012**, 3, 485.
- [44] J. Ilavsky, NIKA analysis system for reduction of 2D SAS data, Version 1.44 (3/3/2010); <http://usaxs.xor.aps.anl.gov/staff/ilavsky/nika.html> (Accessed September, **2011**).
- [45] E. Gann, A. Young, B. A. Collins, H. Yan, J. Nasiatka, H. A. Padmore, H. Ade, A. Hexemer, C. Wang, *Rev. Sci. Instrum.* **2012**, 83, 045110.
- [46] T. J. Prosa, M. J. Winokur, J. Moulton, P. Smith, A. J. Heeger, *Macromolecules* **1992**, 25, 4364.
- [47] J. W. Kiel, B. J. Kirby, C. F. Majkrzak, B. B. Maranville, M. E. Mackay, *Soft Matter* **2010**, 6, 641.